CHEMISTRY OF MATERIALS

pubs.acs.org/cm

Article

Structural Rigidity Control toward Cr^{3+}-Based Broadband Near-Infrared Luminescence with Enhanced Thermal Stability

Gaochao Liu, Maxim S. Molokeev, and Zhiguo Xia*

Cite This: *Chem. Mater.* 2022, 34, 1376−1384

Read Online

ACCESS | Metrics & More | Article Recommendations | Supporting Information

ABSTRACT: Broadband near-infrared (NIR) light sources based on phosphor-converted light-emitting diodes (pc-LEDs) are desirable for biochemical analysis and medical diagnosis applications; however, the development of target NIR phosphor is still a challenge. Herein, broadband NIR phosphors, Cr^{3+}-activated $CaSc_{1-x}Al_{1+x}SiO_6$ (λ_{em} = 950 nm), are designed and optimized by chemical substitution toward enhanced quantum efficiency and thermal stability. Structural and spectral analyses along with density functional theory calculations reveal that Sc^{3+}/Al^{3+} substitution contributes to enhancing the structural rigidity and the local symmetry of the [Sc/AlO_6] octahedron so that the nonradiative relaxation of Cr^{3+} emission centers is suppressed significantly. The as-fabricated phosphor-in-glass-based NIR LED light source demonstrates great potential in the detection of alcohol concentration. This study provides a local structure design principle for exploring NIR phosphors with enhanced thermal stability and will also stimulate further studies on material discovery and quantitative analysis of NIR spectroscopy.

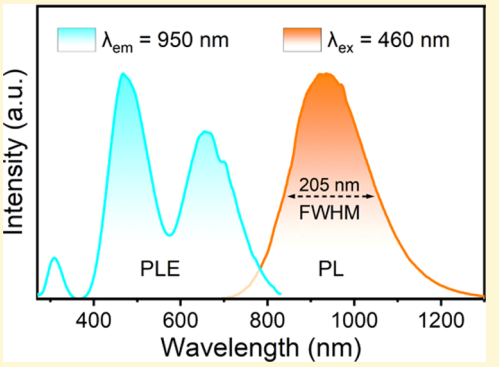

INTRODUCTION

With the rapid development and emerging applications of near-infrared (NIR) spectroscopy in food analysis, medical diagnosis, health monitoring, biosensing, and agriculture, traditional NIR light sources such as halogen lamps are insufficient to meet the diversified demands due to their large volumes, low luminous efficiency, and high operating temperature.[1−3] Accordingly, NIR phosphor-converted light-emitting diodes (pc-LEDs) emerged as the most promising substitutes due to their low cost, good durability, and broad and tunable emission spectra.[4,5] Benefiting from the efficient ultraviolet and blue emissive chips, the greatest challenge for the popularization of NIR pc-LEDs lies in exploring novel broadband NIR phosphors, and extensive efforts have been made presently. For instance, NIR-emitting Eu^{2+}-doped $(Sr,Ba)Y_2O_4$ phosphors have been designed, and giant red-shifted emission from 620 to 773 nm can be realized by chemical substitution.[6] Al^{3+}/Mn^{2+} disorder and $Mn^{2+}−Mn^{2+}$ aggregation in spinel $Mg_{1-x}Al_2O_4$:xMn^{2+} could enable a broadband NIR emission peaking at 825 nm.[7] Ni^{2+} and low-valent Bi ions activated glass materials also exhibit an attractive ultra-broadband NIR emission in the range of 800−1700 nm.[8,9] However, the NIR emission of Eu^{2+} can be hardly shifted to the longer wavelength region by current methods, and the NIR luminescence efficiency of Mn^{2+}, Ni^{2+}, and Bi emission centers is still disappointing,[10] so that the development of target NIR phosphors is still a challenge.

Alternatively, a Cr^{3+} ion has been considered as an ideal NIR activator due to its tunable emission spectrum in a wide region, which strongly depends on the crystal field strength.[11−13] For example, a $Gd_{2.4}Lu_{0.6}Ga_4AlO_{12}:Cr^{3+}$ phosphor was reported for plant growth lighting sources because the efficient NIR emission band peaking at 728 nm matched well with the far-red/phytochrome.[14] $Ca_3Sc_2Si_3O_{12}:Cr^{3+}$ has been demonstrated to have potential in night-vision technology, thanks to its high internal quantum efficiency (IQE) of 92.3% at 700−900 nm.[15] Moreover, the emission peak of $Ga_{2-x}Sc_xO_3:Cr^{3+}$ can be tuned from 720 to 830 nm with a near-unity IQE of 99% for a $Ga_{1.594}Sc_{0.4}O_3$:0.006Cr^{3+} phosphor.[16] Nevertheless, such NIR light may be inappropriate for food component analysis and medical diagnosis applications because most organic functional groups have characteristic absorption for NIR light after 830 nm, and lower-energy photons require larger penetration depth in biotissues due to reduced body autofluorescence and light scattering.[17−19]

Therefore, broadband Cr^{3+}-based NIR phosphors with a long peak emission wavelength (∼>830 nm) and a large full width at half-maximum (FWHM, ∼>200 nm) are still urgently needed. Unfortunately, long-wavelength radiation is usually accompanied by severe nonradiative relaxation and poor thermal resistance since the energy difference between the ground state and excited state of a given emitter is small, which

Received: December 1, 2021
Revised: January 6, 2022
Published: January 19, 2022

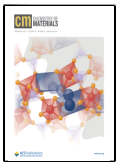

https://doi.org/10.1021/acs.chemmater.1c04131
Chem. Mater. 2022, 34, 1376−1384

is known as the "energy gap law".[20] For example, (Li/Na)In_2SbO_6:Cr^{3+} could give rise to a redshift of its emission band from 970 to 1020 nm along with a broadened FWHM, but its IQE was relatively low.[21] Liu et al. reported Cr^{3+}-doped $Cs_2AgInCl_6$ and $(Mg_{1-x}Li_x)(Mg_{1-x}Sc_x)GeO_4$ NIR phosphors with broad emission bands around 1020 nm but with poor thermal stability.[22,23] Thus, developing Cr^{3+}-doped broadband long-wavelength NIR phosphors with a suppressed nonradiation process and appreciable thermal stability has become a top priority. In this work, we designed a Cr^{3+}-doped $CaScAlSiO_6$ phosphor that exhibits broad NIR emission ranging from 700 to 1300 nm and peaking at 950 nm with a large FWHM of 205 nm under 460 nm excitation. It is found that the IQE and thermal stability of this long-wavelength NIR radiative phosphor could be improved via Sc^{3+}/Al^{3+} chemical substitution in $CaSc_{1-x}Al_{1+x}SiO_6$:$0.01Cr^{3+}$ phosphors. Structural and spectral analyses as well as density functional theory (DFT) calculations suggest that the suppressed nonradiation process of Cr^{3+} emitters in $CaSc_{0.85}Al_{1.15}SiO_6$ may arise from the increased structural rigidity and $[Sc/AlO_6]$ octahedral symmetry. An optimized NIR phosphor-in-glass-based LED (PiG-LED) light source was fabricated remotely, which demonstrates great potential in quantitative detection of alcohol concentration.

EXPERIMENTAL SECTION

Reagents. The reagents used in this study were $CaCO_3$ (99.95%, Aladdin), Li_2CO_3 (99.9%, Aladdin), Sc_2O_3 (99.95%, Macklin), Al_2O_3 (99.99%, Aladdin), SiO_2 (99.99%, Macklin), Cr_2O_3 (99.99%, Aladdin), phosphate glass powder (Z5045, Youhe Chemical Technology Company), and a UV-curable adhesive (Leaftop, 9311). The initial reagents were purchased and used without additional purification.

Synthesis. $CaSc_{1-x}Al_{1+x}SiO_6$:$0.01Cr^{3+}$ ($0 \le x \le 0.15$) samples were synthesized by a high-temperature solid-state reaction method. According to the compositions mentioned above, stoichiometric contents of raw materials and 1 wt % Li_2CO_3 as flux were weighed and ground in an agate mortar for about 10−20 min for complete mixing. The mixtures were decanted into an aluminum oxide crucible and treated in a horizontal tube furnace at 1450 °C for 6 h in a reducing mixed atmosphere of H_2 (5%) and N_2 (95%) to inhibit the formation of Cr^{4+}. Afterward, the tube furnace was cooled to room temperature (RT, 25 °C). The resulting phosphors were ready for use in further measurements.

The PiG sample was prepared by the traditional melt-quenching method. First, the as-prepared $CaSc_{0.85}Al_{1.15}SiO_6$:$0.01Cr^{3+}$ phosphor was ground to below 50 μm and then mixed with the commercial phosphate glass powder, Z5045, in different weight ratios (0:100, 1:99, 3:97, 5:95, and 10:90). The mixtures were ground thoroughly for 10 min, then transferred into corundum crucibles, and put into a muffle furnace to sinter at 800 °C for 15 min in air with continuous stirring to eliminate bubbles. Subsequently, the melt was poured on a graphite mold at 300 °C and annealed for 2 h. After cooling to room temperature with the furnace, the glasses were polished to fine disks with a diameter of 15 mm and a thickness of 1.5 mm for characterizations.

Characterization. Powder X-ray diffraction (PXRD) patterns of all samples were collected at RT by an Aeris XRD diffractometer (PANalytical Corporation, Netherlands) operating at 40 kV and 15 mA with monochromatized Cu Kα radiation (λ = 1.5406 Å) and a linear VANTEC detector. The data were collected in the range of 5−120° with a step size of 0.0217° (2θ) and a count time of 5 s per step. High-quality synchrotron X-ray powder diffraction (SXRD) data were collected at a high-resolution powder diffraction end station with a calibrated wavelength of 0.7789 Å and an energy of 16 keV. Structural characterization and Rietveld refinement were conducted using TOPAS 4.2 software. UV−Vis−NIR transmittance, absorption, and DRS spectra were collected using a Hitachi UH4150 UV−Vis−NIR spectrophotometer at room temperature, in which $BaSO_4$ was used as the reference standard. Room-temperature photoluminescence (PL) spectra and PL excitation (PLE) spectra were recorded using an FLS1000 fluorescence spectrophotometer equipped with a continuous xenon lamp (450 W) as an excitation source and a liquid-nitrogen-cooled NIR photomultiplier tube as a detector (Hamamatsu, R5509, InP/InGaAsP). The PL decay curve was also measured by the same FLS1000 instrument using a microsecond flash lamp (μF900) as the excitation source, and the statistical photons were 5000. The luminescence thermal quenching behavior of the samples was measured by the same spectrophotometer, which was equipped with a TAP-02 high-temperature fluorescence instrument (Tian Jin Orient-KOJI instrument Co., Ltd.). Solid-state ^{27}Al dipole decoupling magic-angle spinning (DD/MAS) nuclear magnetic resonance (NMR) spectra were recorded on an Agilent 600 DD2 spectrometer (Agilent, magnetic field strength 14.1 T) at a resonance frequency of 199.13 MHz for ^{27}Al using high-power 1H decoupling. The powder samples were placed in a pencil-type zirconia rotor of 4.0 mm o.d. The spectra were obtained at a spinning speed of 8 kHz (4 μs 90° pulses) and a recycle delay of 10 s. The Al signal of $NaAlO_2$ was used as the reference of the ^{27}Al chemical shift. The scanning number was 5000. Raman spectra were recorded using a Raman spectrometer (Renishaw in Via, U.K.) equipped with a solid-state laser (532 nm). The quantum yields of $CaScAlSiO_6$:$0.01Cr^{3+}$ and $CaSc_{0.85}Al_{1.15}SiO_6$:$0.01Cr^{3+}$ phosphors at RT were measured by an absolute PL quantum yield spectrometer (Quantaurus-QY Plus C13534-12, Hamamatsu Photonics). Thermographs of the fabricated NIR pc-LED and PiG-LED at different driven currents were taken by a thermal imager (Fotric, 225 S). The pc-LED was fabricated by mixing the $CaSc_{0.85}Al_{1.15}SiO_6$:$0.01Cr^{3+}$ with a UV curing adhesive and coating on a commercial 460 nm LED chip. The PiG-LED was fabricated by coating the corresponding 10 wt %-PiG material on the same blue chip with a graphite cylinder of 12 mm diameter and 50 mm height.

Computational Procedure. The Vienna Ab-initio Simulation Package (VASP) was employed to perform the structural geometry relaxation of the host matrices. The generalized gradient approximation and automatically generated 3 × 3 × 3 k points were employed in the calculations. The energy cutoff of the plane-wave basis was set to 520 eV. The convergence criterion for the electronic energy was 10^{-5} eV, and the structures were relaxed until the Hellmann−Feynman forces were less than −0.01 eV/Å. The Debye temperature (Θ_D) was also estimated using density functional theory (DFT) calculations with the generalized gradient approximation (GGA-PBE) exchange−correlation functional to describe the interactions. An increased plane-wave cutoff energy of 520 eV was used for cell optimization. The electronic iteration convergence was 10^{-5} eV using the normal (blocked Davidson) algorithm and reciprocal space projection operators. An explicit k-mesh of 3 × 3 × 3 was employed.

RESULTS AND DISCUSSION

Crystal Structure of $CaSc_{1-x}Al_{1+x}SiO_6$:$0.01Cr^{3+}$ (x = 0−0.15). The phase purity and crystallinity of the as-prepared $CaSc_{1-x}Al_{1+x}SiO_6$:$0.01Cr^{3+}$ (x = 0, 0.05, 0.10, and 0.15) phosphors were monitored by powder X-ray diffraction (PXRD), and the results are demonstrated in Figure 1a. All peaks were indexed using a monoclinic cell ($C2/c$) with parameters close to $CaScAlSiO_6$ (JCPDS no. 75-1495). The diffraction peaks shift slightly toward a higher angle in the enlarged pattern (2θ = 28.8−30°), illustrating the substitution of Al^{3+} ions for Sc^{3+} other than Si^{4+} due to their difference in effective ionic radius of octahedral coordination ($IR_{Al^{3+}}$ = 0.535 Å < $IR_{Sc^{3+}}$ = 0.745 Å) and tetrahedral coordination ($IR_{Al^{3+}}$ = 0.39 Å > $IR_{Si^{4+}}$ = 0.26 Å).[24] To investigate the detailed structural information of $CaSc_{1-x}Al_{1+x}SiO_6$:$0.01Cr^{3+}$ (x = 0−0.15) phosphors, the $CaScAlSiO_6$ structure was taken

https://doi.org/10.1021/acs.chemmater.1c04131
Chem. Mater. 2022, 34, 1376−1384

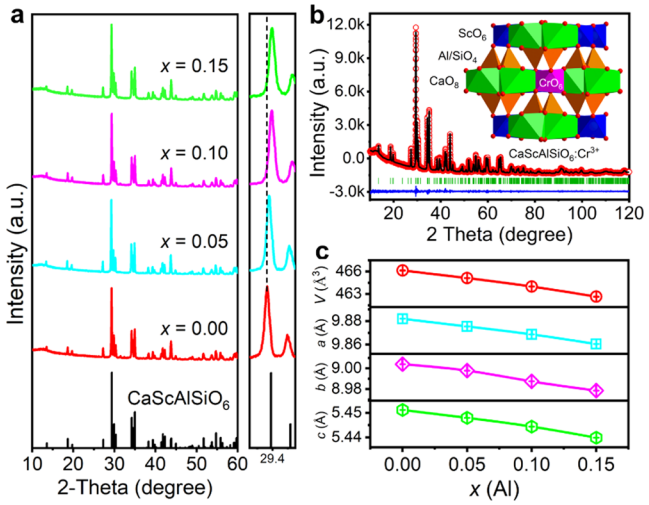

Figure 1. (a) PXRD patterns and the selected diffraction peak near 29.4° of $CaSc_{1-x}Al_{1+x}SiO_6$:0.01Cr^{3+} ($0 \le x \le 0.15$) and the standard pattern of JCPDS card No. 75-1495 for $CaScAlSiO_6$ as a reference. (b) Rietveld refinement result and crystal structure diagram of Cr^{3+}-doped $CaScAlSiO_6$. (c) Refined lattice parameters *V*, *a*, *b*, and *c* of $CaSc_{1-x}Al_{1+x}$ SiO_6:0.01Cr^{3+} as a function of *x*(Al).

as a starting model for Rietveld refinement as shown in Figure 1b,c, which was performed using TOPAS 4.2 software.[25] The results were stable and gave low *R*-factors as listed in Tables S1−S3. The inset in Figure 1b shows the substitution model of Cr^{3+} in the $CaScAlSiO_6$ host that formed by an 8-fold-coordinated Ca^{2+} site, a 6-fold-coordinated Sc^{3+} site, and a 4-fold-coordinated Al^{3+}/Si^{4+} site ($IR_{Cr}{}^{3+}$ = 0.615 Å, $IR_{Ca}{}^{2+}$ = 1.12 Å). It should be noted that the Al^{3+} and Si^{4+} ions are distributed in chains but completely disordered in the crystal lattice, which will be discussed in detail later. Given that the crystal field stabilization energy of Cr^{3+} ions in octahedrons is eight times higher than that in tetrahedrons, the Cr^{3+} ions prefer to occupy the 6-fold-coordinated Sc^{3+} sites based on their close radius and charge balance.[26] With the increase of Al^{3+} content in $CaSc_{1-x}Al_{1+x}SiO_6$:0.01Cr^{3+}, the refined cell parameters *V*, *a*, *b*, and *c* decrease gradually (Figure 1c), which is in line with the shift of diffraction peaks in Figure 1a and emphasizes the $Sc^{3+} \leftrightarrow Al^{3+}$ replacement. However, as the Al^{3+} content keeps increasing ($x > 0.15$), these parameters become irregular because the single phase is hard to form, as shown in Figure S1. Thus, the composition-optimized $CaSc_{1-x}Al_{1+x}SiO_6$:0.01Cr^{3+} (x = 0−0.15) phosphors were further investigated.

Photoluminescence Properties of $CaSc_{1-x}Al_{1+x}SiO_6$:0.01Cr^{3+} (x = 0−0.15). The photoluminescence emission (PL) and photoluminescence excitation (PLE) spectra of $CaScAlSiO_6$:0.01Cr^{3+} at room temperature (RT) are recorded in Figure 2a. Under 460 nm excitation, the phosphor exhibits a broadband emission peaking at 950 nm and ranging from 700 to 1300 nm with a large full width at half-maximum (FWHM) of 205 nm, which should be attributed to the spin-allowed $^4T_2 \rightarrow {}^4A_2$ (^4F) transition of Cr^{3+} ions in octahedral coordination, as mentioned above.[27] Furthermore, a continuous PLE spectrum composed of three bands located at 310, 460, and 670 nm can be acquired when monitoring at the emission maximum, which should be assigned to the $^4A_2 \rightarrow {}^4T_1$ (^4P), $^4A_2 \rightarrow {}^4T_1$ (^4F), and $^4A_2 \rightarrow {}^4T_2$ (^4F) energy level transitions of Cr^{3+} ions, respectively (Figure S2).[28] The UV−Vis−NIR diffuse reflection spectrum (DRS) of the phosphor (Figure S3) indicates that the absorption region is broad and in agreement with the PLE spectrum that matches well with the efficient blue chips.

Given that the valence electrons of Cr^{3+} ions are not shielded by outer shells, there are strong interactions with the crystal field and lattice vibrations due to the spatial extension of the d electron wavefunctions in crystals, and thus it enables variable optical properties of Cr^{3+}-doped phosphors.[23,29] When considering Cr^{3+} ions in the center of coordinated octahedrons (O_h symmetry), the influence of the host lattice on

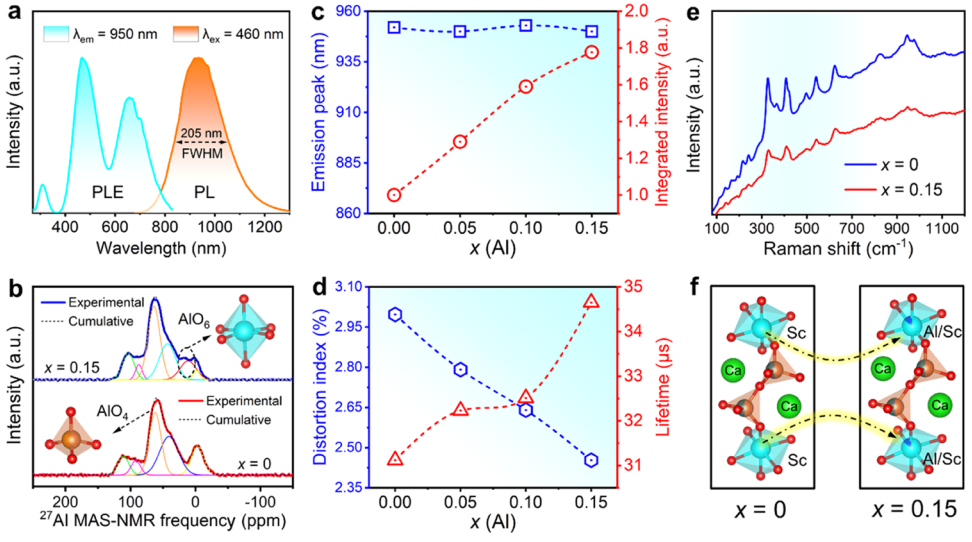

Figure 2. (a) PLE and PL spectra of the $CaScAlSiO_6$:0.01Cr^{3+} phosphor. (b) Solid-state ^{27}Al MAS NMR spectra of $CaSc_{1-x}Al_{1+x}SiO_6$:0.01Cr^{3+} (x = 0 and 0.15). (c) Broadband emission peak and integrated NIR emission intensity of $CaSc_{1-x}Al_{1+x}SiO_6$:0.01Cr^{3+} (x = 0−0.15) phosphors. (d) Distortion index of the [Sc/AlO_6] octahedron and fluorescence lifetime of $CaSc_{1-x}Al_{1+x}SiO_6$:0.01Cr^{3+} (x = 0−0.15) monitored at 950 nm under 460 nm excitation. (e) Raman spectra of the $CaSc_{1-x}Al_{1+x}SiO_6$ (x = 0 and 0.15) host collected under 532 nm laser excitation. (f) Local structural phase transformation model from $CaScAlSiO_6$ to $CaSc_{0.85}Al_{1.15}SiO_6$ via $Sc^{3+} \leftrightarrow Al^{3+}$ substitution.

https://doi.org/10.1021/acs.chemmater.1c04131
Chem. Mater. 2022, 34, 1376−1384

luminescence properties is expressed by certain spectroscopic parameters of D_q, B, and S, which can be roughly estimated by the following equations[30−32]

$$10D_q = E(^4T_2) = E(^4T_2 \rightarrow {}^4T_2) \quad (1)$$

$$B = D_q \frac{y^2 - 10y}{15(y - 8)} \quad (2)$$

where the parameter y is defined as

$$y = \frac{E(^4T_1) - E(^4T_2)}{D_q} = \frac{E(^4A_2 \rightarrow {}^4T_1) - E(^4A_2 \rightarrow {}^4T_2)}{D_q} \quad (3)$$

$$\Delta E_s = (2S - 1)\hbar\omega \quad (4)$$

$$\Gamma(T) = \sqrt{8 \ln 2}\,\hbar\omega \left[S \coth\left(\frac{\hbar\omega}{2kT}\right)\right]^{1/2} \quad (5)$$

In the above equations, D_q is the crystal field strength, $E(^4T_2)$ and $E(^4T_1)$ are the equilibrium positions of the $^4T_2$ (^4F) and $^4T_1$ (^4F) energy levels for Cr^{3+} ions, and E ($^4A_2 \rightarrow {}^4T_2$) and E ($^4A_2 \rightarrow {}^4T_1$) represent the corresponding transition energies, which can be obtained from the PLE spectrum of $CaScAlSiO_6$:0.01Cr^{3+} (Figure 2a). The Racah parameter B means the repulsive force between electrons in the 3d orbital. ΔEs is the Stokes shift of Cr^{3+} luminescence, S represents the Huang−Rhys factor, $\hbar\omega$ is the effective phonon frequency, k means the Boltzmann constant, 0.695 cm^{-1} K^{-1}, and T represents the test temperature (300 K). The crystal field parameter D_q/B was calculated to be 2.07 for $CaScAlSiO_6$:0.01Cr^{3+} (Figure S2), indicating that Cr^{3+} ions are located at a site with a weak crystal field ($D_q/B < 2.3$) so that a broad emission band appears.[33] In addition, the Stokes shift was determined to be 4400 cm^{-1} and significantly larger than that of Cr^{3+} emitters in other hosts.[11,23]

To investigate the origin of the large Stokes shift, the electron−lattice coupling strength reflected by the Huang−Rhys factor S was calculated to be 18.1 on the basis of equations 4 and 5. Apparently, the $CaScAlSiO_6$:0.01Cr^{3+} phosphor suffers from a strong electron−lattice coupling, which is mainly responsible for the long-wavelength broadband NIR radiation.[34−36] However, an overlarge coupling strength will increase the probability of nonradiative relaxation and a lower thermal resistance appears.[11] Thus, appropriate electron−phonon coupling is essential for the high-efficiency long-wavelength NIR emission.

To study the influence of $Sc^{3+} \leftrightarrow Al^{3+}$ substitution on the local crystal structure and optical properties, we first measured the magic-angle spinning (MAS) ^{27}Al solid-state nuclear magnetic resonance (NMR) spectra of $CaSc_{1-x}Al_{1+x}SiO_6$:0.01Cr^{3+} (x = 0 and 0.15), and the results are given in Figure 2b. Obviously, the $CaScAlSiO_6$:0.01Cr^{3+} phosphor exhibits a broad signal ranging from 128 to −30 ppm that consists of five sub-bands located at 111, 92, 62, 41, and −3 ppm, respectively. The complex pattern resulted from aluminum atoms with different chemical environments, which means that there can be between 0 and 4 silicon atoms linked through oxygen bridges to a given aluminum species due to the disordered Al/Si sites in $CaScAlSiO_6$.[37,38] After additional Al^{3+} ions were introduced, another NMR signal of 6-fold-coordinated ^{27}Al located around 11 ppm emerged, while the previous five peaks remained almost unchanged as shown in Table S4,[37] further confirming the $Sc^{3+} \leftrightarrow Al^{3+}$ substitution, which is in accordance with the results of Rietveld refinement in Figure 1. With the increase of x(Al), PL peaks of $CaSc_{1-x}Al_{1+x}SiO_6$:0.01Cr^{3+} phosphors were maintained, while their integrated luminescence intensity increased as shown in Figures 2c and S4, which means that the nonradiative relaxation of Cr^{3+} emitters in $CaSc_{0.85}Al_{1.15}SiO_6$ may be suppressed and will be discussed later. The minor peak at about 970 nm in Figure S4 is caused by the grating defect of the FLS1000 instrument. Under 460 nm excitation, the internal quantum efficiency (IQE) of $CaSc_{1-x}Al_{1+x}SiO_6$:0.01Cr^{3+} (x = 0 and 0.15) is determined to be 21% and 30%, respectively (Figure S4), and the external QE for the latter is only 9% ascribed to the poor absorption ability.

Accordingly, the variation of the local structural distortion of the [Sc/AlO_6] octahedron depending on $Sc^{3+} \leftrightarrow Al^{3+}$ substitution has been discussed to evaluate the structure−property correlation, and it can be described by the following equation[39,40]

$$D_{dis} = \frac{1}{n} \sum_{n}^{i=1} \frac{|d_i - d_{av}|}{d_{av}} \quad (6)$$

where D_{dis} represents the lattice distortion, n is the coordination number, d_i means the distance from Sc to the ith coordinating O atoms, and d_{av} is the average Sc−O distance as shown in Table S3. The calculated D_{dis} values of [Sc/AlO_6] decrease from 3 to 2.45%, as shown in the left of Figure 2d. This means that the structural symmetry increases depending on $Sc^{3+} \leftrightarrow Al^{3+}$ substitution. Moreover, it is well known that the shorter decay time of an emitting center is a characteristic of the distorted surrounding, while longer decay values and better thermal resistance are observed at a symmetrical site.[41] Therefore, the PL decay curves of $CaSc_{1-x}Al_{1+x}SiO_6$:0.01Cr^{3+} (x = 0−0.15) monitored at 950 nm under 460 nm excitation were also recorded at RT as shown in Figure S5a,b. These decay curves can be well fitted by a biexponential function as given below[42]

$$I = A_1 e^{-(t/\tau_1)} + A_2 e^{-(t/\tau_2)} \quad (7)$$

$$\tau_{ave} = \frac{A_1\tau_1^2 + A_2\tau_2^2}{A_1\tau_1 + A_2\tau_2} \quad (8)$$

where I represents the emission intensity, A_1 and A_2 are constants, τ_1 and τ_2 are the decay time for the exponential components, and τ_{ave} is the average decay time. The fitting results of several microseconds are in line with those of typical Cr^{3+}-doped compounds.[43,44] Considering that the $CaSc_{1-x}Al_{1+x}SiO_6$:0.01Cr^{3+} (x = 0 and 0.15) phosphors exhibit a monoexponential decay at low temperatures (Figure S5c,d), the longer τ_2 in Figure S5a,b is regarded as the intrinsic Cr^{3+} ionic luminescence lifetime and the shorter τ_1 may be induced by additional energy decay paths like cross-relaxation or energy migration.[45,46] The fitted average lifetime keeps increasing with the increase of Al^{3+} content as shown in the right part of Figure 2d, which also confirms the presence of more symmetrical [Sc/AlO_6] octahedron, as found by the decreased D_{dis} values.

To further explore the influence of Al^{3+} ions in Sc^{3+} sites on the local structures, Raman spectra of the $CaSc_{1-x}Al_{1+x}SiO_6$ (x = 0 and 0.15) host were measured and compared in Figure 2e. Apparently, the Raman signal of the $CaScAlSiO_6$ host (blue

https://doi.org/10.1021/acs.chemmater.1c04131
Chem. Mater. 2022, 34, 1376−1384

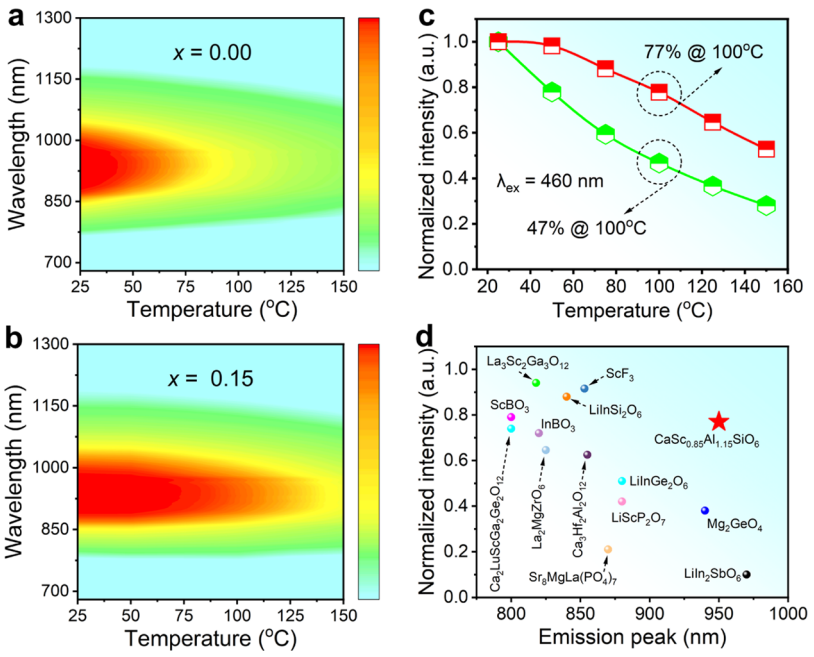

Figure 3. (a,b) PL/temperature correlation maps of $CaSc_{1-x}Al_{1+x}SiO_6$:0.01Cr^{3+} (x = 0 and 0.15) upon 460 nm excitation, respectively. (c) Temperature-dependent integrated emission intensity of $CaScAlSiO_6$:0.01Cr^{3+} (green line) and $CaSc_{0.85}Al_{1.15}SiO_6$:0.01$Cr^{3+}$ (red line). (d) Emission intensity ratios of Cr^{3+}-doped NIR phosphors with different peak positions at 100 °C compared with those at RT.

line) has an intense fluorescence background but weak Raman bands even if there is no Cr^{3+}-doping, which is comparable to previous reports.[47,48] These Raman peaks at 100−300, 300−700, and 700−1000 cm^{-1} are assigned to the ordered $[CaO_8]$, disordered $[Sc/AlO_6]$, and $[Al/SiO_4]$ sites, respectively.[12] After $Sc^{3+} \leftrightarrow Al^{3+}$ substitution, the intensity of these bands become much lower, which means that the lattice vibration of the crystal is weaker and makes it tend to undergo radiative recombination, consistent with the increased emission intensites.[49] In addition, the lattice vibration energy in a crystal is considered to be closely related to its structural rigidity, which can be evaluated theoretically by the Debye temperature (θ_D) according to the following equations[50]

$$\theta_D = \frac{h}{k_B}[6\pi^2 V^{1/2} N]^{1/2} \sqrt{\frac{B_H}{M}} f(\nu) \quad (9)$$

$$f(\nu) = \left\{ \left[2\left(\frac{2}{3}\cdot\frac{1+\nu}{1-2\nu}\right)^{3/2} + \left(\frac{1}{3}\cdot\frac{1+\nu}{1-\nu}\right)^{3/2} \right]^{-1} \right\}^{1/3} \quad (10)$$

where k_B and h are the Boltzmann constant and Planck constant, respectively. M means the molecular mass of the compound, B_H represents the adiabatic bulk modulus of the crystal, N means the number of atoms per unit cell, ν is the Poisson ratio, and V is the volume of the unit cell. Considering the complexity of the crystal structure after Sc^{3+} ions were substituted partly, the Debye temperature of $CaScAlSiO_6$ and $CaSc_{0.875}Al_{1.125}SiO_6$ were calculated to be 596 and 623 K, respectively. These θ_D values are much higher than those of other Cr^{3+}-doped NIR phosphors such as $GaTaO_4$ (567 K), ScF_3 (534 K), and $LiInSi_2O_6$ (550 K).[19] The increased θ_D is in line with the change of Raman spectra and will also contribute to the thermal resistance as discussed later. The structural transition model from $CaScAlSiO_6$ to $CaSc_{0.85}Al_{1.15}SiO_6$ via substitution of Sc^{3+} by Al^{3+} is shown in Figure 2f. Although the Al^{3+} and Si^{4+} ions occupy the same crystallographic sites in $CaScAlSiO_6$, excessive Al^{3+} ions prefer to enter the 6-fold-coordinated Sc^{3+} sites, enabling a more constricted crystal lattice and strengthening bond forces between different ions so that the structural rigidity of the crystal is improved.

Temperature-Dependent PL Properties. Generally, the high structural rigidity of the host material will inhibit soft phonon modes that lead to the nonradiative relaxation of activators, and an excellent thermal quenching resistance can be observed for the phosphor.[51] Therefore, temperature-dependent PL spectra of $CaSc_{1-x}Al_{1+x}SiO_6$:0.01Cr^{3+} (x = 0 and 0.15) phosphors under 460 nm excitation were measured and are depicted in Figure 3a,b, respectively. Obviously, the luminescence thermal stability of Cr^{3+} ions in $CaScAlSiO_6$ was improved greatly after $Sc^{3+} \leftrightarrow Al^{3+}$ substitution, which was mainly attributed to the suppressed nonradiative relaxation process that was induced by the improvement of the structural rigidity and local symmetry of the $[Sc/AlO_6]$ octahedron as analyzed previously. Figures 3c and S6 display the normalized temperature-dependent integrated emission intensity of $CaSc_{1-x}Al_{1+x}SiO_6$:0.01Cr^{3+} (x = 0−0.15), which shows the detailed thermal stability of these phosphors. At 100 °C, 47% of the NIR emission intensity at RT can be maintained for $CaScAlSiO_6$:0.01Cr^{3+} (green line) and 77% of that for $CaSc_{0.85}Al_{1.15}SiO_6$:0.01$Cr^{3+}$ (red line). The optimized thermal stability is much better than other Cr^{3+}-doped long-wavelength broadband NIR phosphors as shown in Figure 3d.[11,12,21,23,35,36,44,52−57]

NIR PiG-LED Fabrication. Although the thermal resistance of Cr^{3+} ions in $CaScAlSiO_6$ was improved significantly via Al^{3+}/Sc^{3+} substitution, the traditional coating package was not applicable for the phosphor. On the one hand, the commercial blue chips will generate abundant heat when operating under a heavy current that causes luminescence quenching of the phosphor. On the other hand, the organic adhesives may age easily at high temperatures and have a certain characteristic absorption band in the NIR region (Figure S7). Hence, a

https://doi.org/10.1021/acs.chemmater.1c04131
Chem. Mater. 2022, 34, 1376−1384

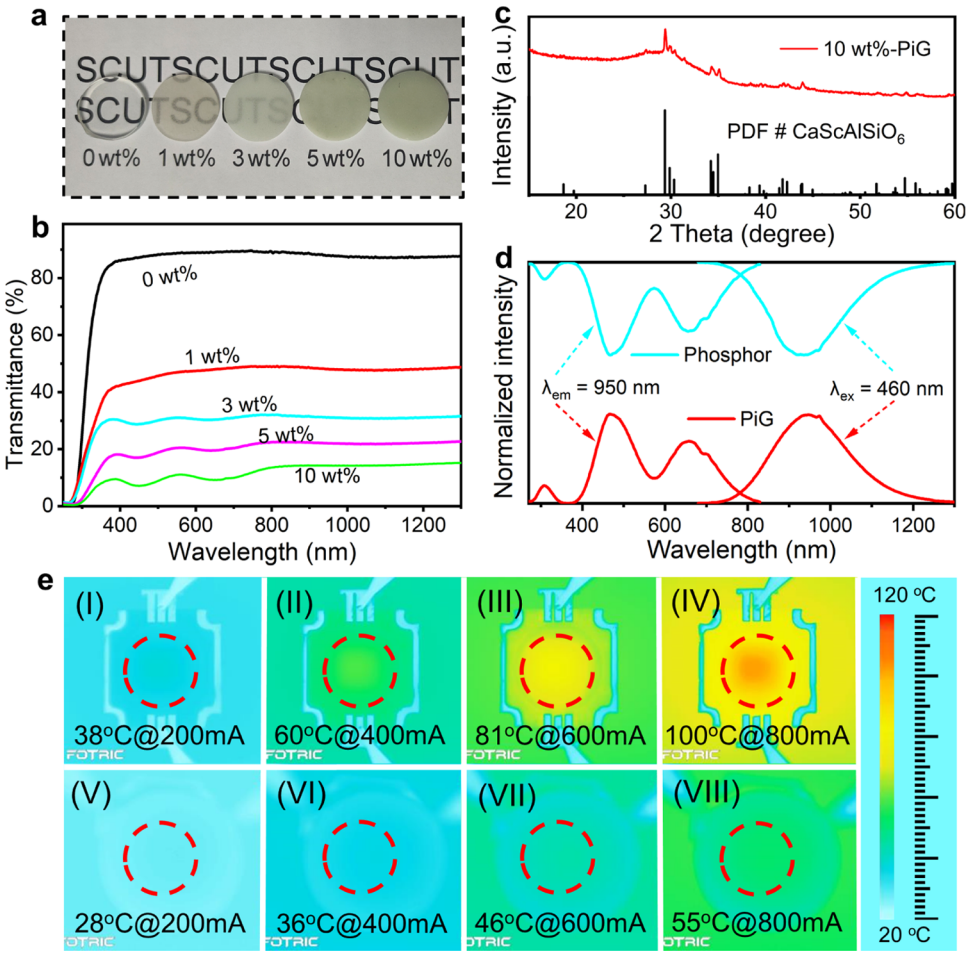

Figure 4. (a, b) Flat disks and total transmittance of $CaSc_{0.85}Al_{1.15}SiO_6$:0.01$Cr^{3+}$-PiG with various phosphor contents (15 mm in diameter and 1.5 mm in thickness). (c) XRD patterns of 10 wt %-PiG and standard pattern of $CaSAlSiO_6$ as the reference. (d) Excitation and emission spectra of the $CaSc_{0.85}Al_{1.15}SiO_6$:0.01$Cr^{3+}$ powder and 10 wt %-PiG. (e) Thermographs of the fabricated NIR pc-LED (I-IV) and PiG-LED (V−VIII) at different driven currents from 200 to 800 mA.

phosphor-in-glass (PiG) material for remote packaging was prepared by mixing the $CaSc_{0.85}Al_{1.15}SiO_6$:0.01$Cr^{3+}$ phosphor with a commercial phosphate glass powder as shown in Figure 4a,b. Apparently, pure phosphate glass exhibits considerable transmittance for visible and NIR light, implying that full densification is achieved. By incorporating the $CaSc_{0.85}Al_{1.15}SiO_6$:0.01$Cr^{3+}$ powder into the glass, the as-synthesized samples become translucent gradually owing to light scattering. Nevertheless, moderate light scattering is beneficial to color uniformity and light extraction of high-power PiG-based LEDs (PiG-LEDs), especially when laser diodes (LDs) are used as the excitation source.[58] In addition, the XRD patterns, PL, and PLE spectra as well as the thermal stability of the prepared 10 wt %-PiG are in accord with those of the pure phosphor powder as shown in Figures 4c,d and S8, indicating that the glass has little effect on the phase and spectral profile of the $CaSc_{0.85}Al_{1.15}SiO_6$:0.01$Cr^{3+}$ powder. Consequently, NIR pc-LED and PiG-LED were fabricated for comparison by coating the phosphor and 10 wt %-PiG material on a commercial InGaN blue chip (460 nm), respectively. Their thermographs at different driven currents from 200 to 800 mA are shown in Figure 4e (I−VIII). With the increase of driven currents to 800 mA, the working temperature of pc-LED rises significantly from 38 to 100 °C due to the close contact between the phosphor and the chip, which will cause thermal quenching of the fabricated NIR phosphor as shown in Figure 3c. However, this drawback can be well overcome by extending the distance between the blue chip and the emitters, which means a remote packaging as depicted in Figure 5a. When the distance is enlarged to 50 mm, the operating temperature of the fabricated NIR PiG-LED can be reduced to 55 °C driven under an 800 mA current (Figure 4e, VIII) so that a thermally stable NIR output can be acquired.

Quantitative Analysis of Alcohol Concentration. It is well known that the C−H, N−H, O−H, and other functional groups with various energy levels in organic molecules can absorb NIR light in common with their own vibrational frequency, so that the NIR absorption spectrum of each molecule is a fingerprint.[23] Accordingly, organic component detection based on NIR light sources can be used to quickly analyze multiple chemical compositions. Herein, a model sample designed using mixtures with a concentration gradient of absolute alcohol and distilled water was prepared to establish the relationship between the alcohol concentration and the spectral signal. The schematic diagram and test results are shown in Figure 5. Driven by an 800 mA current, the 10 wt %-PiG converted the blue light of the InGaN chip to broadband NIR light, which was detected by an InP/InGaAsP detector after passing through various mixed solutions with a proportion of absolute alcohol from 0 to 100% with an interval

https://doi.org/10.1021/acs.chemmater.1c04131
Chem. Mater. 2022, 34, 1376−1384

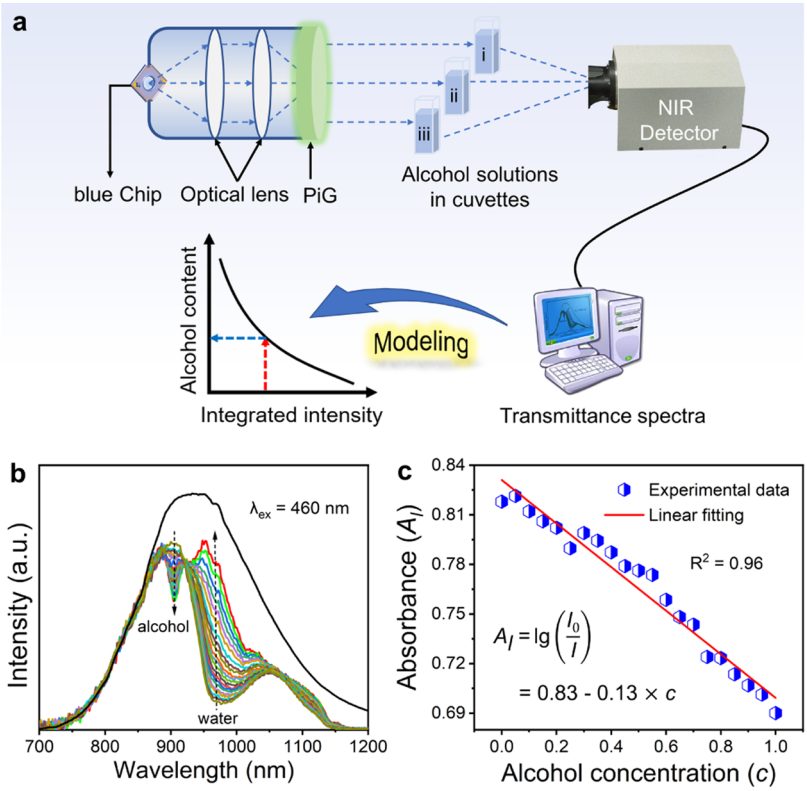

Figure 5. (a) Schematic illustration of the construction of the blue InGaN chip-driven NIR light device to detect alcohol concentration. (b) NIR transmittance spectra using the NIR light emitted from 10 wt %-PiG penetrating a series of mixed solutions of water and alcohol in different proportions. The signal intensity of the black line was reduced three times for comparison. (c) Functional relationship between alcohol concentration and NIR light absorbance.

of 5%. The transmittance spectra are displayed in Figure 5b containing two distinguished absorption bands peaking at 930 and 970 nm compared with the original PL spectrum, which should be attributed to the characteristic absorption of alcohol and water, respectively.[44] Furthermore, the intensity of the response at 930 nm increased with the rise of ethanol concentration, and their relationship was established based on the Lambert−Beer law[59]

$$A_l = \lg\left(\frac{I_0}{I}\right) = \varepsilon l c \tag{11}$$

where A_l represents the absorbance of a certain component in a transparent solution and ε means its molar absorptivity, l is the optical path length during the test (50 mm for this work), and c represents the concentration of the light-absorbing component in the solution. I_0 and I are the original and transmissive intensity of the monochromatic light. Hence, the concentration c can be calculated directly according to the law if I_0 and I are obtained. As for the broadband light source, the corresponding integrated intensity can be used for analysis. Therefore, the original transmittance spectral data of the mixed solutions were used to establish a functional model between alcohol concentration and absorbance as shown in Figure 5c. These results can be well fitted by a linear relationship with a satisfactory R^2 value of 96%. Consequently, the alcohol concentration in a mixed solution of absolute alcohol and distilled water with unknown proportions can be estimated based on the fitted function, and only a transmittance spectrum of the solution needs to be measured. Although the functional model is applicable only for mixed solutions composed of absolute alcohol and distilled water, it provides an avenue for the exploration of NIR spectroscopy technology in the quantitative analysis of different organic solvents in the future.

CONCLUSIONS

In conclusion, Cr^{3+}-doped $CaSc_{1-x}Al_{1+x}SiO_6$ phosphors (λ_{em} = 950 nm) were designed, and simultaneous emission and thermal resistance enhancements were realized via Sc/Al substitution. Structural and spectral analyses along with DFT calculations suggest that the nonradiative relaxation of Cr^{3+} emitters in $CaSc_{0.85}Al_{1.15}O_6$ was suppressed significantly via the $Sc^{3+} \leftrightarrow Al^{3+}$ substitution, which should be attributed to the enhanced structural rigidity and the local symmetry of the [Sc/AlO_6] octahedron. Finally, a PiG-LED based on the newly discovered NIR phosphors was fabricated remotely to further diminish the device operating temperature current, which demonstrates great potential in the quantitative analysis of alcohol concentration. This work offers a new design principle toward the performance optimization of Cr^{3+}-based near-infrared phosphors for new photonic applications.

ASSOCIATED CONTENT

Supporting Information

The Supporting Information is available free of charge at https://pubs.acs.org/doi/10.1021/acs.chemmater.1c04131.

Tables S1−S4 and Figures S1−S7 showing the detailed Rietveld refinement results, SXRD patterns, decay curves, and additional PL data (PDF)

https://doi.org/10.1021/acs.chemmater.1c04131
Chem. Mater. 2022, 34, 1376−1384

AUTHOR INFORMATION

Corresponding Author

Zhiguo Xia − *The State Key Laboratory of Luminescent Materials and Devices, Guangdong Provincial Key Laboratory of Fiber Laser Materials and Applied Techniques, School of Materials Science and Engineering, South China University of Technology, Guangzhou 510640, China; School of Physics and Optoelectronics, South China University of Technology, Guangzhou 510641, China;* orcid.org/0000-0002-9670-3223; Email: xiazg@scut.edu.cn

Authors

Gaochao Liu − *The State Key Laboratory of Luminescent Materials and Devices, Guangdong Provincial Key Laboratory of Fiber Laser Materials and Applied Techniques, School of Materials Science and Engineering, South China University of Technology, Guangzhou 510640, China*

Maxim S. Molokeev − *Laboratory of Crystal Physics, Kirensky Institute of Physics, Federal Research Center KSC SB RAS, Krasnoyarsk 660036, Russia; Siberian Federal University, Krasnoyarsk 660041, Russia; Department of Physics, Far Eastern State Transport University, Khabarovsk 680021, Russia;* Present Address: Research and Development Department, Kemerovo State University, Kemerovo 650000, Russia; orcid.org/0000-0002-8297-0945

Complete contact information is available at: https://pubs.acs.org/10.1021/acs.chemmater.1c04131

Notes

The authors declare no competing financial interest.

ACKNOWLEDGMENTS

This work was supported by the International Cooperation Project of the National Key Research and Development Program of China (2021YFE0105700), National Natural Science Foundation of China (Nos.: 51972118 and 51961145101), Guangzhou Science & Technology Project (202007020005), and the Local Innovative and Research Teams Project of Guangdong Pearl River Talents Program (2017BT01X137). This work was also funded by RFBR according to the research Project No. 19-52-80003.

REFERENCES

(1) Qiao, J. W.; Zhou, G. J.; Zhou, Y. Y.; Zhang, Q. Y.; Xia, Z. G. Divalent Europium-Doped Near-Infrared-Emitting Phosphor for Light-Emitting Diodes. *Nat. Commun.* **2019**, *10*, No. 5267.

(2) Wang, C. P.; Wang, X. M.; Zhou, Y.; Zhang, S.; Li, C.; Hu, D. F.; Xu, L.; Jiao, H. An Ultra-Broadband Near-infrared Cr^{3+}-Activated Gallogermanate $Mg_3Ga_2GeO_8$ Phosphor as Light Sources for Food Analysis. *ACS Appl. Electron Mater.* **2019**, *1*, 1046−1053.

(3) Wu, Q.; Li, Pl.; Ye, Z. J.; Huo, X. X.; Yang, H. F.; Wang, Y.; Wang, D. W.; Zhao, J. X.; Yang, Z. P.; Wang, Z. J. Near-infrared Emitting Phosphor $LaMg_{0.5}(SnGe)_{0.5}O_3:Cr^{3+}$ for Plant Growth Applications: Crystal Structure, Luminescence, and Thermal Stability. *Inorg. Chem.* **2021**, *60*, 16593−16603.

(4) Yang, Z. Y.; Zhou, Y. Y.; Qiao, J. W.; Molokeev, M. S.; Xia, Z. G. Rapid Synthesis of Red-Emitting $Sr_2Sc_{0.5}Ga_{1.5}O_5:Eu^{2+}$ Phosphors and the Tunable Photoluminescence Via Sr/Ba Substitution. *Adv. Opt. Mater.* **2021**, *9*, No. 2100131.

(5) Zhong, J. Y.; Zhuo, Y.; Du, F.; Zhang, H. S.; Zhao, W. R.; Brgoch, J. Efficient and Tunable Luminescence in $Ga_{2-x}In_xO_3:Cr^{3+}$ for Near-infrared Imaging. *ACS Appl. Mater. Interfaces* **2021**, *13*, 31835−31842.

(6) Yang, Z. Y.; Zhao, Y. F.; Zhou, Y. Y.; Qiao, J. W.; Chuang, Y. C.; Molokeev, M. S.; Xia, Z. G. Giant Red-Shifted Emission in $(Sr,Ba)Y_2O_4:Eu^{2+}$ Phosphor toward Broadband Near-infrared Luminescence. *Adv. Funct. Mater.* **2021**, No. 2103927.

(7) Song, E. H.; Jiang, X. X.; Zhou, Y. Y.; Lin, Z. S.; Ye, S.; Xia, Z. G.; Zhang, Q. Y. Heavy Mn^{2+} Doped $MgAl_2O_4$ Phosphor for High-Efficient Near-infrared Light-Emitting Diode and the Night-Vision Application. *Adv. Opt. Mater.* **2019**, *7*, No. 1901105.

(8) Xiong, P. X.; Li, Y. Y.; Peng, M. Y. Recent Advances in Super Broad Infrared Luminescence Bismuth-Doped Crystals. *iScience* **2020**, *23*, No. 101578.

(9) Yu, G.; Wang, W.; Jiang, C. Linear Tunable NIR Emission via Selective Doping of Ni^{2+} Ion into ZnX_2O_4 (X=Al, Ga, Cr) Spinel Matrix. *Ceram. Int.* **2021**, *47*, 17678−17683.

(10) Gao, Y.; Wang, B.; Liu, L.; Shinozaki, K. Near-Infrared Engineering for Broad-Band Wavelength-Tunable in Biological Window of NIR-II and -III A Solid Solution Phosphor of $Sr_{1-x}Ca_xTiO_3:Ni^2$. *J. Lumin.* **2021**, *238*, No. 118235.

(11) Malysa, B.; Meijerink, A.; Jüstel, T. Temperature Dependent Cr^{3+} Photoluminescence in Garnets of the Type $X_3Sc_2Ga_3O_{12}$ (X = Lu, Y, Gd, La). *J. Lumin.* **2018**, *202*, 523−531.

(12) Zhang, L. L.; Wang, D. D.; Hao, Z. D.; Zhang, X.; Pan, Gh.; Wu, H. J.; Zhang, J. H. Cr^{3+}-Doped Broadband NIR Garnet Phosphor with Enhanced Luminescence and Its Application in NIR Spectroscopy. *Adv. Opt. Mater.* **2019**, *7*, No. 1900185.

(13) He, F. Q.; Song, E. H.; Zhou, Y. Y.; Ming, H.; Chen, Z. T.; Wu, J. C.; Shao, P. S.; Yang, X. F.; Xia, Z. G.; Zhang, Q. Y. A General Ammonium Salt Assisted Synthesis Strategy for Cr^{3+}-Doped Hexafluorides with Highly Efficient Near Infrared Emissions. *Adv. Funct. Mater.* **2021**, *31*, No. 2103743.

(14) Zou, X. K.; Wang, X. J.; Zhang, H. R.; Kang, Y. Y.; Yang, X.; Zhang, X. J.; Molokeev, M. S.; Lei, B. F. A Highly Efficient and Suitable Spectral Profile Cr^{3+}-Doped Garnet Near-infrared Emitting Phosphor for Regulating Photomorphogenesis of Plants. *Chem. Eng. J.* **2022**, *428*, No. 132003.

(15) Jia, Z. W.; Yuan, C. X.; Liu, Y. F.; Wang, X.-J.; Sun, P.; Wang, L.; Jiang, H. C.; Jiang, J. Strategies to Approach High Performance in Cr^{3+}-Doped Phosphors for High-Power NIR-LED Light Sources. *Light Sci. Appl.* **2020**, *9*, 86.

(16) Fang, M.-H.; Chen, K.-C.; Majewska, N.; Leśniewski, T.; Mahlik, S.; Leniec, G.; Kaczmarek, S. M.; Yang, C.-W.; Lu, K.-M.; Sheu, H.-S.; Liu, R.-S. Hidden Structural Evolution and Bond Valence Control in Near-infrared Phosphors for Light-Emitting Diodes. *ACS Energy Lett.* **2021**, *6*, 109−114.

(17) Tian, R.; Ma, H. L.; Yang, Q. L.; Hao, Wan.; Zhu, S. J.; Chandra, S.; Sun, H. T.; Kiesewetter, D. O.; Niu, G.; Liang, Y. Y.; Chen, X. Y. Rational Design of a Super-Contrast NIR-II Fluorophore Affords High-Performance NIR-II Molecular Imaging Guided Microsurgery. *Chem. Sci.* **2019**, *10*, 326−332.

(18) Workman, J. J. Interpretive Spectroscopy for Near Infrared. *Appl. Spectrosc. Rev.* **1996**, *31*, 251−320.

(19) Zhong, J. Y.; Zhuo, Y.; Du, F.; Zhang, H. S.; Zhao, W. R.; You, S. H.; Brgoch, J. Efficient Broadband Near-infrared Emission in the $GaTaO_4:Cr^{3+}$ Phosphor. *Adv. Opt. Mater.* **2021**, No. 2101800.

(20) Wei, Y.-C.; Wang, S. F.; Hu, Y.; Liao, L.-S.; Chen, D.-G.; Chang, K.-H.; Wang, C.-W.; Liu, S.-H.; Chan, W.-H.; Liao, J.-L.; Hung, W.-Y.; Wang, T.-H.; Chen, P.-T.; Hsu, H.-F.; Chi, Y.; Chou, P.-T. Overcoming the Energy Gap Law in Near-infrared OLEDs by Exciton−Vibration Decoupling. *Nat. Photonics* **2020**, *14*, 570−577.

(21) Liu, G. C.; Hu, T.; Molokeev, M. S.; Xia, Z. G. Li/Na Substitution and Yb^{3+} Co-Doping Enabling Tunable Near-infrared Emission in $LiIn_2SbO_6:Cr^{3+}$ Phosphors for Light-Emitting Diodes. *iScience* **2021**, *24*, No. 102250.

(22) Zhao, F. Y.; Song, Z.; Zhao, J.; Liu, Q. L. Double Perovskite $Cs_2AgInCl_6:Cr^{3+}$: Broadband and Near-infrared Luminescent Materials. *Inorg. Chem. Front.* **2019**, *6*, 3621−3628.

(23) Cai, H.; Liu, S. Q.; Song, Z.; Liu, Q. L. Tuning Luminescence from NIR-I to NIR-II in Cr^{3+}-Doped Olivine Phosphors for Nondestructive Analysis. *J. Mater. Chem. C* **2021**, *9*, 5469−5477.

(24) SHANNON, R. D. Revised Effective Ionic Radii and Systematic Studies of Interatomie Distances in Halides and Chaleogenides. *Acta Cryst.* **1976**, *A32*, 751−767.
(25) Bruker *AXS TOPAS V4: General Profile and Structure Analysis Software for Powder Diffraction Data—User's Manual*; Bruker AXS: Karlsruhe, Germany, 2008.
(26) Lai, J. A.; Qiu, J. B.; Wang, Q.; Zhou, D. C.; Long, Z. W.; Yang, Y.; Hu, S. H.; Li, X. Z.; Pi, J. C.; Wang, J. Disentangling Site Occupancy, Cation Regulation, and Oxidation State Regulation of the Broadband Near Infrared Emission in a Chromium-Doped $SrGa_4O_7$ Phosphor. *Inorg. Chem. Front.* **2020**, *7*, 2313−2321.
(27) Yuan, C. X.; Li, R. Y.; Liu, Y. F.; Zhang, L. L.; Zhang, J. H.; Leniec, G.; Sun, P.; Liu, Z. H.; Luo, Z. H.; Dong, R.; Jiang, J. Efficient and Broadband $LiGaP_2O_7:Cr^{3+}$ Phosphors for Smart Near-infrared Light-Emitting Diodes. *Laser Photonics Rev.* **2021**, *15*, No. 2100227.
(28) Liu, C. Y.; Xia, Z. G.; Chen, M. Y.; Molokeev, M. S.; Liu, Q. L. Near-infrared Luminescence and Color Tunable Chromophores Based on Cr^{3+}-Doped Mullite-Type $Bi_2(Ga,Al)_4O_9$ Solid Solutions. *Inorg. Chem.* **2015**, *54*, 1876−1882.
(29) Adachi, S. Review—Photoluminescence Properties of Cr^{3+}-Activated Oxide Phosphors. *ECS J. Solid State Sci. Technol.* **2021**, *10*, No. 026001.
(30) Tanabe, Y. On the Absorption Spectra of Complex Ions Ii. *J. Phys. Soc. Jpn.* **1954**, *9*, 766−779.
(31) Torchia, G. A.; Matos, O. M.; Vaveliuk, P.; Tocho, J. O. Electron−Lattice Coupling in Congruent Co-Doped $LiNbO_3:Cr^{3+}$:ZnO Crystal. *J. Phys.: Condens. Matter* **2001**, *13*, 6577−6583.
(32) Su, B. B.; Li, M. Z.; Song, E. H.; Xia, Z. G. Sb^{3+}-Doping in Cesium Zinc Halides Single Crystals Enabling High-Efficiency Near-infrared Emission. *Adv. Funct. Mater.* **2021**, *31*, No. 2105316.
(33) De Guzman, G. N. A.; Fang, M.-H.; Liang, C.-H.; Bao, Z.; Hu, S.-F.; Liu, R.-S. Near-Infrared Phosphors and Their Full Potential: A Review on Practical Applications and Future Perspectives. *J. Lumin.* **2020**, *219*, No. 116944.
(34) Liu, D. J.; Li, G. G.; Dang, P. P.; Zhang, Q. Q.; Wei, Y.; Lian, H. Z.; Shang, M. M.; Lin, C. C.; Lin, J. Simultaneous Broadening and Enhancement of Cr^{3+} Photoluminescence in $LiIn_2SbO_6$ by Chemical Unit Cosubstitution: Night-Vision and Near-infrared Spectroscopy Detection Applications. *Angew. Chem. Int. Ed. Engl.* **2021**, *60*, 14644−14649.
(35) Yao, L. Q.; Shao, Q. Y.; Han, S. Y.; Liang, C.; He, J. H.; Jiang, J. Q. Enhancing near-Infrared Photoluminescence Intensity and Spectral Properties in Yb^{3+} Codoped $LiScP_2O_7:Cr^{3+}$. *Chem. Mater.* **2020**, *32*, 2430−2439.
(36) Sun, Z. S.; Ning, Q. X.; Zhou, W. Y.; Luo, J. B.; Chen, P. C.; Zhou, L. Y.; Pang, Q.; Zhang, X. G. Structural and Spectroscopic Investigation of an Efficient and Broadband NIR Phosphor $InBO_3:Cr^{3+}$ and Its Application in NIR Pc-LEDs. *Ceram. Int.* **2021**, *47*, 13598−13603.
(37) Pena, P.; Rivas Mercury, J. M.; de Aza, A. H.; Turrillas, X.; Sobrados, I.; Sanz, J. Solid-State ^{27}Al and ^{29}Si NMR Characterization of Hydrates Formed in Calcium Aluminate−Silica Fume Mixtures. *J. Solid State Chem.* **2008**, *181*, 1744−1752.
(38) Lentz, P.; Carvalho, A. P.; Delevoye, L.; Fernandez, C.; Amoureux, J.-P.; Nagy, J. B. Characterization of Offretite During Hydrothermal Treatment by High-Resolution Solid-State ^{29}Si Magic Angle Apinning Nmr and ^{27}Al Tripe-Quantum Magic Angle Apinning NMR Spectroscopy. *Magn. Reson. Chem.* **1999**, *37*, S55−S62.
(39) Baur, W. H. The Geometry of Polyhedral Distortions. Predictive Relationships for the Phosphate Group. *Acta Cryst.* **1974**, *30*, 1195−1215.
(40) Chen, M. Y.; Molokeev, M. S.; Lin, C. C.; Su, C.; Chuang, Y.-C.; Liu, Q. L. Probing Eu^{2+} Luminescence from Different Crystallographic Sites in $Ca_{10}M(PO_4)7:Eu^{2+}$ (M = Li, Na, and K) with β-$Ca_3(PO_4)_2$-Type Structure. *Chem. Mater.* **2017**, *29*, 7563−7570.
(41) Gao, T. Y.; Zhuang, W. D.; Liu, R. H.; Liu, Y. H.; Yan, C. P.; Chen, X. X. Design of a Broadband NIR Phosphor for Security-Monitoring LEDs: Tunable Photoluminescence Properties and Enhanced Thermal Stability. *Cryst. Growth Des.* **2020**, *20*, 3851−3860.
(42) Wang, C. P.; Zhang, Y. X.; Han, X.; Hu, D. F.; He, D. P.; Wang, X. M.; Jiao, H. Energy Transfer Enhanced Broadband Near-infrared Phosphors: Cr^{3+}/Ni^{2+} Activated $ZnGa_2O_4−Zn_2SnO_4$ Solid Solutions for the Second NIR Window Imaging. *J. Mater. Chem. C* **2021**, *9*, 4583−4590.
(43) Liu, G. C.; Molokeev, M. S.; Lei, B. F.; Xia, Z. G. Two-Site Cr^{3+} Occupation in the $MgTa_2O_6:Cr^{3+}$ Phosphor toward Broad-Band Near-infrared Emission for Vessel Visualization. *J. Mater. Chem. C* **2020**, *8*, 9322−9328.
(44) Xu, X.; Shao, Q.; Yao, L.; Dong, Y.; Jiang, J. Highly Efficient and Thermally Stable Cr^{3+}-Activated Silicate Phosphors for Broadband Near-infrared LED Applications. *Chem. Eng. J.* **2020**, *383*, No. 123108.
(45) Bachmann, V.; Ronda, C.; Oeckler, O.; Schnick, W.; Meijerink, A. Color Point Tuning for $(Sr,Ca,Ba)Si_2O_2N_2:Eu^{2+}$ for White Light LEDs. *Chem. Mater.* **2009**, *21*, 316−325.
(46) Yu, D. C.; Zhou, Y. S.; Ma, C. S.; Melman, J. H.; Baroudi, K. M.; LaCapra, M.; Riman, R. E. Non-Rare-Earth $Na_3AlF_6:Cr^{3+}$ Phosphors for Far-Red Light-Emitting Diodes. *ACS Appl. Electron. Mater.* **2019**, *1*, 2325−2333.
(47) Ma, C.; Rossman, G. R. Davisite, $CaScAlSiO_6$, a New Pyroxene from the Allende Meteorite. *Am. Mineral.* **2009**, *94*, 845−848.
(48) Sekita, M.; Ohashi, H.; Terada, S. Raman Spectroscopic Study of Clinopyroxenes in the System $CaScAlSiO_6$ - $CaAl_2SiO_6$. *Phys. Chem. Minerals* **1988**, *15*, 319−322.
(49) Han, P. G.; Mao, X.; Yang, S. Q.; Zhang, F.; Yang, B.; Wei, D. H.; Deng, W. Q.; Han, K. L. Lead-Free Sodium-Indium Double Perovskite Nanocrystals through Doping Silver Cations for Bright Yellow Emission. *Angew. Chem. Int. Ed. Engl.* **2019**, *58*, 17231−17235.
(50) Qiao, J. W.; Zhao, J.; Liu, Q. L.; Xia, Z. G. Recent Advances in Solid-State LED Phosphors with Thermally Stable Luminescence. *J. Rare Earths* **2019**, *37*, 565−572.
(51) Zhuo, Y.; Mansouri Tehrani, A.; Oliynyk, A. O.; Duke, A. C.; Brgoch, J. Identifying an Efficient, Thermally Robust Inorganic Phosphor Host Via Machine Learning. *Nat. Commun.* **2018**, *9*, No. 4377.
(52) Bai, B.; Dang, P. P.; Huang, D. Y.; Lian, H. Z.; Lin, J. Broadband near-Infrared Emitting $Ca_2LuScGa_2Ge_2O_{12}:Cr^{3+}$ Phosphors: Luminescence Properties and Application in Light-Emitting Diodes. *Inorg. Chem.* **2020**, *59*, 13481−13488.
(53) Shao, Q. Y.; Ding, H.; Yao, L. Q.; Xu, J. F.; Liang, C.; Jiang, J. Q. Photoluminescence Properties of a $ScBO_3:Cr^{3+}$ Phosphor and Its Applications for Broadband Near-infrared LEDs. *RSC Adv.* **2018**, *8*, 12035−12042.
(54) Lin, Q. M.; Wang, Q.; Liao, M.; Xiong, M. X.; Feng, X.; Zhang, X.; Dong, H. F.; Zhu, D. Y.; Wu, F. G.; Mu, Z. F. Trivalent Chromium Ions Doped Fluorides with Both Broad Emission Bandwidth and Excellent Luminescence Thermal Stability. *ACS Appl. Mater. Interfaces* **2021**, *13*, 18274−18282.
(55) Zeng, H. T.; Zhou, T. L.; Wang, L.; Xie, R.-J. Two-Site Occupation for Exploring Ultra-Broadband Near-infrared Phosphor—Double-Perovskite $La_2MgZrO_6:Cr^{3+}$. *Chem. Mater.* **2019**, *31*, 5245−5253.
(56) Liu, T. Y.; Cai, H.; Mao, N.; Song, Z.; Liu, Q. L. Efficient Near-infrared Pyroxene Phosphor $LiInGe_2O_6:Cr^{3+}$ for NIR Spectroscopy Application. *J. Am. Ceram. Soc.* **2021**, *104*, 4577−4584.
(57) Malysa, B.; Meijerink, A.; Jüstel, T. Temperature Dependent Photoluminescence of Cr^{3+} Doped $Sr_8MgLa(PO_4)_7$. *Opt. Mater.* **2018**, *85*, 341−348.
(58) Li, S. X.; Wang, L.; Hirosaki, N.; Xie, R. J. Color Conversion Materials for High-Brightness Laser-Driven Solid-State Lighting. *Laser Photonics Rev.* **2018**, *12*, No. 1800173.
(59) Swinehart, D. F. The Beer-Lambert Law. *J. Chem. Educ.* **1962**, *39*, 333−335.

https://doi.org/10.1021/acs.chemmater.1c04131
Chem. Mater. 2022, 34, 1376−1384